IUTAM Symposium on Understanding Common Aspects of Extreme Events in Fluids

Fibonacci patterns: common or rare?

A. C. Newell, M. Pennybacker*

University of Arizona, Department of Mathematics, P.O. Box 210089, Tucson, AZ 85721, USA

Abstract

Using a partial differential equation model derived from the ideas of the Meyerowitz and Traas groups on the role of the growth hormone auxin and those of Green and his group on the role compressive stresses can play in plants, we demonstrate how all features of spiral phyllotaxis can be recovered by the passage of a pushed pattern forming front. The front is generated primarily by a PIN1 mediated instability of a uniform auxin concentration and leaves in its wake an auxin fluctuation field at whose maxima new primordia are assumed to be initiated. Because it propagates through a slowly changing metric, the patterns have to make transitions between spirals enumerated by decreasing parastichy numbers. The point configurations of maxima coincide almost exactly with those configurations generated by the use of discrete algorithms based on optimal packing ideas which suggests that pushed pattern forming fronts may be a general mechanism by which natural organisms can follow optimal strategies.

© 2013 The Authors. Published by Elsevier Ltd.
Selection and peer-review under responsibility of the School of Mathematical Sciences, University College Dublin
Keywords: Phyllotaxis; Pattern Formation; Optimal Packing

1. Introduction

Plant patterns, involving the arrangement of phylla (flowers, leaves, bracts, florets) and the surface morphologies in the vicinity of shoot apical meristems, have intrigued scientists for at least four hundred years. It is only in recent years that rational explanations have emerged which begin to come to terms with the variety of configurations (Fibonacci spirals, whorls) and shapes (almost hexagonal, rhombic, ridgelike) which are observed. The purpose of this paper is to present stunning new evidence that all of the features of phyllotactic configurations are the result of a pushed pattern-forming front whose origin is a combination of biochemically and mechanically induced instabilities. The pushed pattern-forming front is the solution of a pattern forming partial differential equation (PFPDE) and is closely connected with equations derived in [1] which are informed by the pioneering ideas of Meyerowitz, Traas et al and Green et al [2, 3, 4] on the biochemical and mechanical mechanisms which are responsible for the instabilities. The front leaves in its wake either whorls or Fibonacci spirals. The patterns we observe exhibit all known self-similar properties associated with spiral phyllotaxis and reveal some new invariants. What is absolutely remarkable is that the maxima of the pattern field coincide almost exactly with the point configurations generated by discrete algorithms which reflect optimal packing strategies, the bases for a class of teleological explanations. The ramifications of such

---

* Corresponding author.
 E-mail address: pennybacker@math.arizona.edu

a coincidence are potentially very important because they illustrate how an organism can follow an optimal strategy, such as a plant placing the next new flower in the most open space on the generative annulus near its shoot apical meristem (SAM), by employing nonequilibrium instability generated patterns. The results also suggest circumstances under which Fibonacci patterns can be considered universal. They can arise and be long-lived in many physical contexts. We will outline those circumstances in which they are common and not rare. Finally, we make a number of nontrivial predictions which can in principle and in practice be tested experimentally.

The outline of this paper is as follows. In Section 2, we discuss in more detail the nature of the explanations for phyllotactic patterns and introduce the equation whose pushed pattern-forming fronts we investigate. The algorithm is nontrivial and introduces a discretization of the free energy and the variational derivative, which preserves the dissipative property of the gradient flow. In Section 3, we present the results in considerable detail. We also present nontrivial outcomes which should be experimentally testable. In Appendix Appendix A, we describe the numerical method we use in detail.

2. Explanations for phyllotaxis

There are two categories of explanations. The first we call teleological (X is so in order that Y... e.g. tigers have stripes in order to be better camouflaged) in that there are rules which reflect the idea that each new primordium (initial stage of a phyllum) is placed according to a least crowded or optimal packing criterion which presumably gives it most access to light and nutrients. But plants do not have any obvious on-board computers to make such choices. So how is it that a plant can achieve such an outcome? To answer this, we turn to the second category of explanation which we call the mechanistic. Incidentally one of the pioneers of self-organized behaviors, D'Arcy Thompson, spoke eloquently in his classic work *On Growth and Form* on the question of these two kinds of explanations. In this second category of explanation, we try to identify the physical and biochemical processes which lead plants to choose certain phyllotactic configurations and which give rise to the morphologies seen on plant surfaces (hexagonal, rhombic and ridge shapes). As we have said in the introduction, the absolutely remarkable fact is that the predicted outcomes of both explanations are very, very similar which leads to the intriguing suggestion that pattern forming systems which lay down their patterns annulus-by-annulus do so in a way so as to achieve optimal packing. Even D'Arcy Thompson, most definitely an advocate for the second category of explanation, did grant the possibility that there was some merit to the first kind by remarking "Like warp and woof, mechanism and teleology are interwoven together, and we must not cleave to the one and despise the other." Rather similar to another comparison in literature, this one due to Rudyard Kipling, "For the Colonel's Lady an' Judy O'Grady / Are sisters under their skins!"

2.1. Teleological

We divide the teleological explanation of phyllotaxis again into two categories: static models and dynamic models. In each category, phylla are represented as points on a cylinder or a disc. Static models consider the plant only after it is fully grown and predict the selected phyllotactic arrangement by optimizing a lattice of phylla with respect to some quantity, such as packing efficiency, contact pressure or entropy. Dynamic models capture the time evolution of the arrangement by specifying some rule for laying down phylla individually so as to locally optimize a similar quantity. Arrangements predicted by static models often manifest as long-time behavior of dynamic models, when repeated local optimization leads to global optimization. However, dynamic models tend to consider primarily the relaxation to these fixed points and only briefly consider how the pattern of points laid down changes continuously as some key parameter changes slowly in space-time.

The purpose of this section is to outline some of the key ideas in the static and dynamic models, to recount some of the history and to discuss their predictions.

2.1.1. Static models

One of the first mathematical approaches to the problem of phyllotaxis was due to Van Iterson [5]. His idea was that leaves on a stem could be approximated by identical circular discs on the surface of a cylinder, with no overlapping, so that their centers form a regular lattice. The density of a particular lattice may be quantified by the packing efficiency η, defined to be the proportion of the surface of the cylinder covered by discs with the maximum possible radius. The
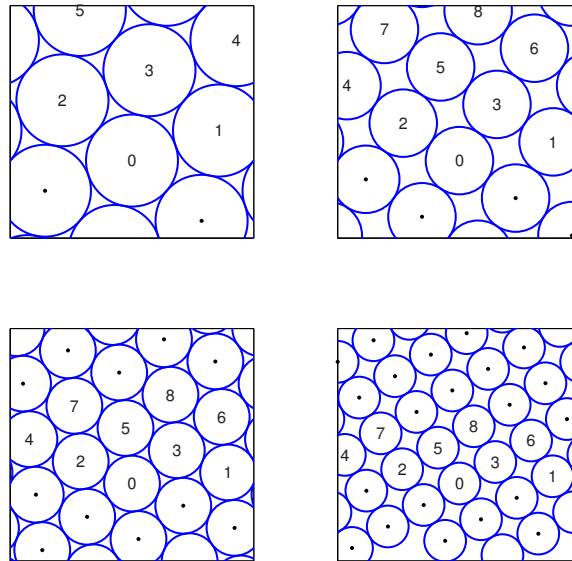
Fig. 1. Four examples of cylindrical lattices and their associated packings. The lattices on the left are hexagonal with $(m,n,m+n)$ being $(1,2,3)$ on the top and $(2,3,5)$ on the bottom. The lattices on the right are rhombic with (m,n) being $(2,3)$ on the top and $(3,5)$ on the bottom. Selected lattice points have been labeled according to their axial ordering.

lattice selected by the plant would be the one which gives the most efficient packing. He also observed that we need only to consider simple lattices, in which no two points lie at the same axial position. A cylindrical lattice that is not simple may be split into an integer number of identical lattices that are simple.

By 1911, it had been known for over a century that a close hexagonal packing is densest among regular arrangements on the plane, but Van Iterson encountered the following problem: simple hexagonal lattices are not always possible on the cylinder. To illustrate this fact, consider the situation illustrated in the upper left lattice of Figure 1. If we take the vector separating the points labelled 0 and 1, it is not difficult to see that the entire lattice is generated by integer multiples of this vector, wrapping around the cylinder as needed. This implies that each simple lattice must have a single generative spiral running through every lattice point, with consecutive lattice points separated by a constant axial distance ρ and angle δ. Choosing either of these quantities arbitrarily, in general, results in a lattice that is not hexagonal. In fact, there are only countably many ρ and δ that yield hexagonal lattices. Furthermore, if we index the points consecutively along the generative spiral of a simple hexagonal lattice, for instance, the indices of the nearest neighbors must be related as $(m,n,m+n)$ with $\gcd(m,n)=1$. We choose $m < n$ by convention. Each lattice on the left of Figure 1 is an illustration of a simple hexagonal lattice. Notice that the hexagonal lattice is not perfectly aligned with the axis of the cylinder. This is not unusual, since otherwise the lattice would not be simple in almost every case.

We define the term n-parastichy as being the family of spirals winding through every n-th point in a lattice. For instance, in either lattice of Figure 1 the 2-parastichy consists of a spiral through the centers of discs 0 and 2 and another parallel spiral through the centers of discs 1, 3, and 5. It is possible to draw an n-parastichy for any n by connecting lattice points whose indices differ by n. On the other hand, there are only two or three parastichies that are most visible. These are the ones formed by connecting each point with its nearest neighbors. It is customary to refer to a lattice by its two most visible parastichies, given by the two nearest neighbors or each point. In the upper left lattice of Figure 1, the most visible parastichies are exactly the neighbors 1, 2 and 3, so we may refer to this as a $(1,2)$, $(1,3)$, $(2,3)$, or $(1,2,3)$ lattice. In general, when the lattice is not hexagonal, the parastichy numbers of the lattice will be uniquely defined.

Of course, our goal is to understand the variety of patterns observed on plants. The true value of ρ is related to the growth rate of the plant and the time between the formation of new primordia, both of which vary between different
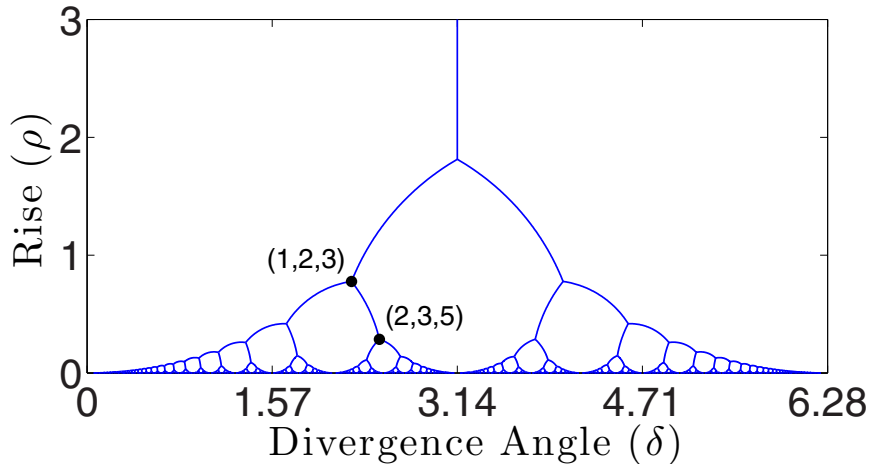
Fig. 2. The Van Iterson diagram of rhombic cylindrical lattices, in terms of their rise and divergence angle. The lattices previously shown in Figure 1 have been marked.

plant species, different specimens of the same plant species, and even over the lifetime of a single specimen. It is certainly not restricted to values that guarantee the existence of a hexagonal lattice, so we must investigate how to maintain a dense packing between hexagonal states. Consider the situation illustrated in Figure 1. If we think of the transition from one hexagonal packing to the next as an axial compression, resulting from a decrease of ρ, then we can imagine the $(m,n) = (1,2)$ to $(m,n) = (2,3)$ transition as the disc centered at point 5 slipping between discs 2 and 3 to touch disc 0. We could also imagine disc 4 slipping between discs 1 and 3 to form $(m,n) = (1,3)$. These correspond to transitions in parastichy numbers $(1,2) \rightarrow (2,3) \rightarrow (3,5)$ and $(1,2) \rightarrow (1,3) \rightarrow (3,4)$ respectively. In general, Van Iterson showed that any (m,n) hexagonal lattice can compress symmetrically to either $(m,m+n)$ or $(n,m+n)$ and that during the transition the densest lattice is rhombic, in that the two nearest neighbors remain equidistant. The set of all possible rhombic cylindrical lattices is illustrated in Figure 2. Each bifurcation point in this tree diagram corresponds to a hexagonal lattice, for which each point is preceded by three equidistant nearest neighbors, and the two branches in decreasing ρ correspond to the two transition possibilities described above. Each segment connecting the bifurcation points corresponds to a continuum of rhombic lattices, each having the same parastichy numbers. Note that the choice of divergence angle δ for a fixed rise ρ is not unique. Different Fibonacci-like sequences lead to different divergence angles, with different angular differences δ between successive lattice points.

More recently, Levitov [6] discovered similar lattice structures among flux vortices in layered superconductors. The vortices would organize into arrays due to a repulsive potential, and these arrays obeyed an analogous transition rule. He also demonstrated that, for a large class of repulsive potentials, the bifurcation points are no longer symmetric: the branch including the larger of the indices is energetically preferred, with the consequence that, in most cases, the lattice structure (m,n) of an array will fall along the sequence of successive Fibonacci numbers. We will also find this to be the case for the mechanistic models.

2.1.2. Dynamic models

A major criticism of the static models of phyllotaxis is that the plant does not spring fully formed from the earth, but instead grows bit-by-bit from the shoot apical meristem (SAM). The SAM is already present at the tip of the plant embryo, which is contained within the seed and has many rapidly dividing cells. Primordia initiate at the edge of the meristem, and as the plant grows, the meristem moves upward and leaves behind previously formed phylla. The botanist Wilhelm Hofmeister published one of the earliest studies of meristems [7] and, from his careful observations, he proposed the following heuristic for primordium formation:

1. The meristem is axisymmetric.
2. Primordia form in a generative annulus on the periphery of the apex.

3. New primordia form at regular time intervals.

4. Primordia move radially away from the apex.

5. Each new primordium forms in the least crowded spot left by the existing primordia.

These rules provided the basis for almost all dynamic models, although the fixed time periodicity was relaxed by Snow and Snow [8].

In a pioneering series of works, Douady and Couder [9, 10, 11] showed via experiments that an algorithm incorporating the Hofmeister rules gives rise to much of what was observed on plants. They designed a laboratory experiment in which uniform drops of ferrofluid were periodically dispensed at the center of an circular oil-filled dish. A radial magnetic field gradient caused the drops to experience an outward force, which resulted in radial motion away from the center. The drops were also mutually repulsive, so each drop moved into the least crowded spot. They found that by varying the time period between drops, proportional to the rise parameter ρ, and the strength of the magnetic field, spirals corresponding to different members of the Fibonacci sequence were formed. Subsequent numerical simulations were used to refine their results.

More recently, a discrete dynamical system was proposed by Atela, Golé, and Hotton in order to put the Hofmeister rules in a more geometrical framework [12]. As in the static models, the surface of the stem may be approximated by a cylinder. The phase space for the dynamical system is the set of sequences of points $\{\mathbf{z}_m = (z_m, \theta_m) \mid m \in \mathbb{N}\}$ on the cylinder, where $z_m = m \cdot \rho$ for a fixed positive number ρ called the rise. The points in any sequence represent the positions of primordia on the cylinder, each primordium residing at a unique level z_m. The primordium at $\mathbf{z}_m$ may be thought of as the m-th oldest primordium. The dynamical system, defined by its action on the elements of a sequence, takes $(z_m, \theta_m) \rightarrow (z_{m+1}, \theta_m)$. That is, each step moves every primordium up one level while having no effect on its angular coordinate. To complete the definition of the map, however, we need to determine the angular coordinate of the point $\mathbf{z}_0 = (0, \theta_0)$. The idea is that θ_0 should be chosen so that $\mathbf{z}_0$ appears in the "least crowded spot." The crowdedness of a spot can be quantified by the distance to the nearest primordium, so let $d(\mathbf{z}_m, \mathbf{z}_n)$ be the Euclidean distance on the cylinder between points $\mathbf{z}_m$ and $\mathbf{z}_n$. The distance from a new primordium with angular coordinate θ_0 to its nearest neighbor is given by

$$D(\theta_0) = \min_{m>0} d(\mathbf{z}_0, \mathbf{z}_m).$$

Hofmeister's least crowded spot is given by the maximum of D over all angular coordinates θ_0. The earlier works by Douady and Couder [9, 10, 11] and Levitov [6] instead assigned to each primordium an inhibitory potential, and the least crowded spot was determined by minimizing the net potential over θ_0. These models yield identical results for a potential of the form d^{-s} in the limit $s \rightarrow \infty$.

A main result of [12] is that, neglecting arbitrary rotation, simple lattices are asymptotically stable fixed points of this dynamical system. Two criteria are primarily responsible for the selection of fixed point lattices. Due to the fact that d is locally convex, the location of each new primordium is equidistant from two existing primordia. As a result, the fixed-point lattice is rhombic. Additionally, the location of each new primordium has an angular coordinate between the two nearest primordia. One says therefore that the lattice is opposed. It is therefore rhombic, opposed, simple lattices that are stable fixed points of the dynamical system. The rhombic condition implies a fixed point diagram identical to the optimal packing results of Van Iterson, and the opposedness condition breaks the symmetry of the bifurcation points as in the case of Levitov. In other words, the $(n, m+n)$ branch in the Van Iterson diagram of Figure 2 is preferred over the $(m, m+n)$ branch. For a given value of ρ, the fixed point could lie on one of many branches of the Van Iterson diagram, but once on a branch it remains there so long as ρ varies adiabatically. So, in most cases, the long-time behavior of this model will result in lattice structures (m, n) that fall along the sequence of successive Fibonacci numbers.

2.2. Mechanical

The problem with the teleological explanation is that, whereas they may tell us why a plant might choose the phyllotactic configurations it does, it does not tell us how the plant achieves this outcome. Saying that it is genetically preprogrammed does not help much. If the program is indeed contained in a plant's DNA, then an explanation

requires a description of the steps which take instructions written at nanoscales to instructions which are manifested at millimeter scales, an order of magnitude greater than typical cell sizes. Mechanistic explanations on the other hand look for self-organization features which are driven by physical and biochemical processes which occur on length scales not too different from those connected with the observed outcomes. It is this approach which we now describe.

In [1, 13], we formulated a description of the neighborhood of the SAM which took account of both the elastic and biochemical natures of the tunica (the plant's skin). In building the combined model, we used the facts that the tunica was a curved elastic shell subject to differential and auxin generated growth stresses and at the same time supported nonuniform concentrations of the auxin growth hormone. Green and coworkers [4] were among the first to propose that differential growth induced compressive stresses in the generative annulus were responsible for a buckling pattern and that stress inhomogeneities gave rise to some unspecified biochemical action which initiated primordium growth. Later work by Reinhardt and colleagues [3] indicated that the presence or absence of auxin at certain locations gave rise to enhanced or depleted growth at those locations. In two pioneering works, the groups of Meyerowitz [2] at Caltech and Traas [3] in Paris, showed that quasiperiodic patterns of auxin concentration could be induced by an instability involving PIN1 proteins. In most equilibrium situations, chemical concentrations are smoothed out by diffusion. But the situation in plants is not an equilibrium one. PIN1 proteins in the interior of cells move under the influence of an auxin gradient into cell walls where they orient so as to drive auxin with, rather than against, its concentration gradient. When the effect is sufficiently strong so as to overcome ordinary diffusion, the net negative diffusion leads to an instability. The balance between linear losses of auxin concentration to the plant corpus, negative second order and ordinary fourth order diffusion leads to an instability threshold and a preferred instability length scale. In the model we built, we took advantage of the fact that that length was long compared to cell diameters and converted, via a continuum field approximation, the discrete cell-by-cell dynamics of the Meterowitz-Traas description into a partial differential equation [1]. The influence of stress on growth (a widespread phenomenon in most organisms which has yet to be understood) was modelled by adding to the equation for the growth induced strain a term proportional to the trace of the stress tensor (a macroscopic measure of the "pulling apart" of cells which helps growth).

The net result is a set of three coupled partial differential equations (PDE's) for $w(\mathbf{x},t)$, $f(\mathbf{x},t)$ and $g(\mathbf{x},t)$, respectively the normal deformation to the overdamped elastic surface, the Airy stress potential and the growth strain associated with the fluctuation of auxin about its mean level. The first attempt to analyze solutions of these equations focused on near onset conditions, namely when the negative diffusion and circumferential stress were close to their threshold values for instability to occur. The analysis was carried out by dividing the set of all shapes and configurations into active (that set of modes $\mathscr{A}$ which were linearly unstable or neutral) and passive (those modes slaved to the active modes by a center manifold graph $\mathscr{P}(\mathscr{A})$) modes. The amplitudes of the active modes are the order parameters of the system, and the PDE's were replaced by equations for these complex amplitudes. Near onset, the amplitude equations are a gradient flow even if the original PDE's are not. Among the main features we found were:

(i) As a function of the radius r of the generative annulus, there was a continuous locus of energy minima corresponding to Fibonacci patterns.

(ii) The amplitude equations satisfied self-similar properties whereby the amplitudes $a_{m_j}(r)$ of the active modes satisfied $a_{m_j}(r) = a_{m_{j+1}}(r\varphi)$ and the radial wavenumbers $\ell_{m_j}(r)$ satisfied $\ell_{m_j}(r) = -\ell_{m_{j+1}}(r\varphi)$ where φ is the golden number $(1+\sqrt{5})/2$.

(iii) If only the auxin instability was initiated, the surface shapes were slaved to the auxin fluctuation field pattern and corresponding phyllotactic configurations but if both instabilities were active, then it was possible for the surface mode shapes to be dominated by ridges while the phyllotactic configurations remained approximately hexagonal or rhombic.

Whereas the near onset analysis was encouraging, it is less than satisfactory on three counts. First, it assumes that the key parameters, in this case either the amount of reverse diffusion of auxin or compressive stresses or a combination of both, have values at the threshold of instability. Whereas one might make a case that this should be so, there is no evidence that it is. Second, and this is a criticism which may also be leveled at the discrete algorithms, the analysis assumes that the system responds adiabatically to changes in what is the key variable, namely the radius of the annulus at which the new primordium formation takes place. We fix the radius and then calculate the sequence

of amplitudes and radial wavenumbers which minimize the free energy at that radius value. We then assume that if the loci of the minima change continuously, then the system with changing radius will follow those loci. Whereas we will show that this is indeed what happens, we do not know this a priori.

Third, we do not know that the points which the amplitude equations identify as energy minima, derived from projecting the actual field onto a truncated set of Fourier modes, will be minima for the original PDE. What the numerical results will in fact tell us is that while these points are critical points of the true energy functional, they are unstable with strongly attracting stable manifolds and weakly repelling unstable ones. The physical reason is that when the pattern is fully filled in over a large region, it cannot distinguish locally the fact that it is not on the plane, and therefore it attempts to access the true energy minimum for the plane, which is a lattice of hexagons. In the case of the sunflower seed pattern, the Fibonacci pattern will, over a very long time, develop defect structures. We discuss this behavior in detail in section 3.6. In actual plants, there is in all likelihood a rooting mechanism which will freeze the pattern after it is set. But for the pattern which evolves from the pushed front of the PDE, we have to be aware that the fixed point is not a true minimum but a saddle with a weak unstable manifold.

What we do, therefore, is numerically simulate the PDE's which govern the process. In this first work, we simplify the model by assuming (a) that the surface deformations are slaved to the auxin concentration field and that the pattern is mainly the result of the Meyerowitz-Traas instability, and (b) that we can ignore the terms in the governing equation which are non-gradient. The remaining PDE is given by

$$\frac{\partial u}{\partial t} = \mu u - \left(\nabla^2 + 1\right)^2 u - \frac{\beta}{3}\left(|\nabla u|^2 + 2u\nabla^2 u\right) - u^3 \tag{1}$$

and the energy by

$$\mathscr{E}[u] = -\int \frac{\mu}{2}u^2 - \frac{1}{2}\left(u + \nabla^2 u\right)^2 + \frac{\beta}{3}u|\nabla u|^2 - \frac{1}{4}u^4. \tag{2}$$

Despite being given these simplifications, the simulation of (1) is nontrivial, especially as we want to follow the pattern front from radii at which the dominant parastichies are 144 and 89 down to radii at which they are 5 and 3. In Appendix Appendix A, we describe how to construct a numerical method to achieve both stability and accuracy.

3. Results

3.1. Discussion of how sunflower seeds form, motivation for the choices of quantities we measure, comments on fronts and the nature of the energy landscape

We study solutions of (1) in many geometries defined by surfaces of revolution $r = r(z)$, for example $r'(z) = 0$ on a cylinder and $r'(z) = 1$ on a disc, but in this paper we focus on what we call the sunflower situation in a disc geometry. Sunflowers are formed in two stages. In the first stage, flowers are initiated in a generative annulus surrounding the plant's SAM and, as the plant grows, the generative annulus and the region of phylla (manifested as flowers) move further out, and their configurations evolve into spiral families. At a certain point, however, the center region consisting of mushy undifferentiated cells begins to undergo a phase transition and, from the outside in, creates florets or seeds. In this process, the seeds are laid down annulus-by-annulus by an inwardly moving front and the particular pattern which forms at a given radius stays at that radius. This means that any optimal packing property which the pattern manifests when it is first laid down remains visible. The diameter of the plant when the process is completed (over a time scale of several days) in of the order of millimeters. Thereafter the plant grows adiabatically until it reaches its mature diameter of 10-15 cm. To simulate this situation, we initiate a spiral pattern with parastichy numbers (m,n) in a circle of radius $m+n$. Our choices of starting parastichies are $(89,144)$ and $(76,123)$ which are consecutive members of the Fibonacci-like sequences starting with $(1,2)$ and $(1,3)$ respectively. We then allow the pattern to propagate inward according to (1) and analyze the resulting field $u(\mathbf{x},t)$.

Guided by previous analytical results at near-onset conditions, we understood several key points. First is the fact that Fibonacci spirals, and indeed whorl structures, are very much a consequence of the presence of a sign reversal asymmetry and the fact that the pattern is laid down by a moving front annulus by annulus in an environment of slowly changing metric. The asymmetry gives hexagonal lattices a special role in planar patterns because modes $\exp(i\mathbf{k}_m \cdot x)$,
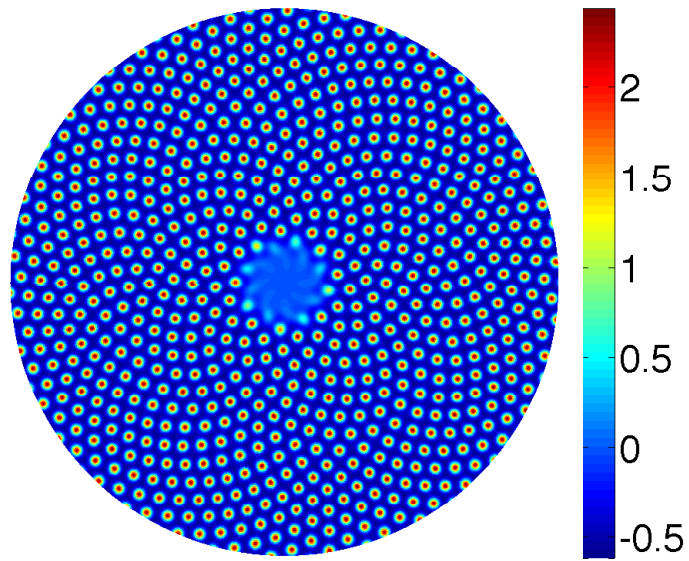
Fig. 3. A pseudocolor plot of $u(\mathbf{x},t)$ on the section $r < 89$ of a pattern initiated at $r = 233$ with parastichy numbers $(89, 144)$. A movie may be found at `http://math.arizona.edu/~pennybacker/media/sunflower/`.
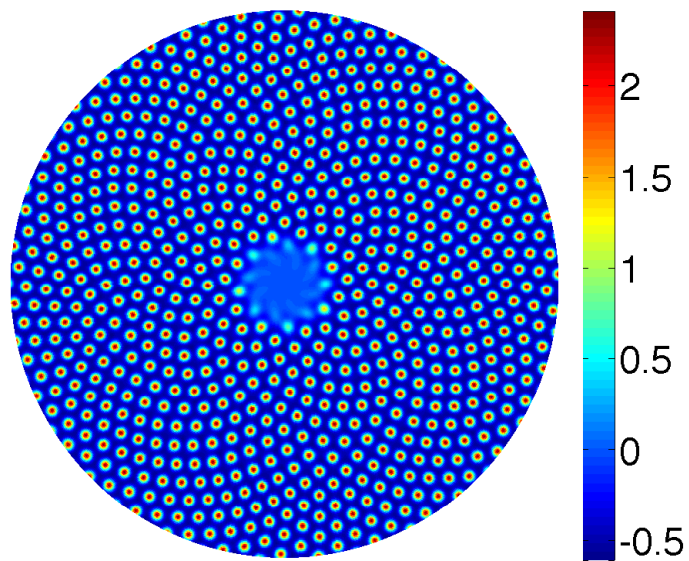

Fig. 4. A pseudocolor plot of $u(\mathbf{x},t)$ on the section $r < 89$ of a pattern initiated at $r = 199$ with parastichy numbers $(76, 123)$.
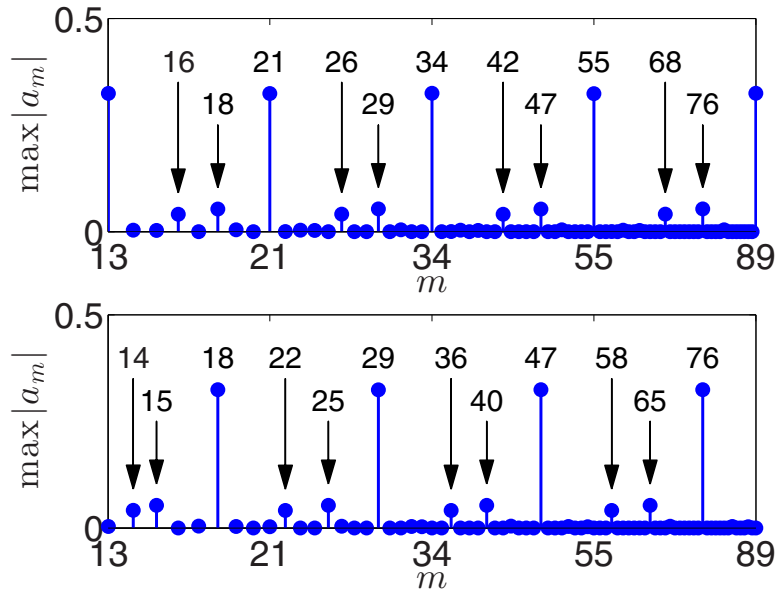
Fig. 5. The maximum values of the amplitude of all integer modes $8 \leq m \leq 89$, with a subset of circumferential wavenumbers indicated. The top figure corresponds to the $(1,2)$ sunflower and the bottom to the $(1,3)$ sunflower.

having $\mathbf{k}_m = k_0$, with wavevectors 120 degrees apart reinforce each other via quadratic interactions. Likewise, in a circular geometry, for patterns laid down annulus by annulus, we observe triads of modes having wavevectors $\mathbf{k}_m = (m, \ell_m)$, $\mathbf{k}_n = (n, \ell_n)$, $\mathbf{k}_{m+n} = \mathbf{k}_m + \mathbf{k}_n$ with shapes $exp(-i \int \ell_m dr - im\theta)$, a good approximation for r large, m/r finite. The signs of successive radial wavenumbers alternate. These modes can reinforce each other via quadratic interactions at certain radii where they have almost equal amplitudes and energetically preferred wavenumbers, with lengths given by $\mathbf{k}_m^2 = \ell_m^2 + m^2/r^2$. But, as the radius increases, the lengths of the wavevectors begin to deviate from their optimal values. Moreover, the energetically preferred radial wavenumbers $(\ell_m(r), \ell_n(r))$ evolve along a computable locus. As a consequence, the first three of the new quadratically generated modes, $\mathbf{k}_{2m}$, $\mathbf{k}_{2n}$, $\mathbf{k}_{2m+n}$ move away from, whereas the last wavevector, $\mathbf{k}_{m+2n}$, moves towards the critical circle. This results in the amplitudes of the first three modes being slaved to, and much less than, the amplitude of the last (see Fig. 5). Thus, in situations where the pattern is laid down annulus by annulus, the quadratic interactions select from the set of all integers only that subset obeying Fibonacci rules. In Fig. 6, we show how the set of wavevectors move as r decreases. It vividly displays the selection process. Note that the pattern in the $(1,2)$ case is almost hexagonal at $r = 13$ and $r = 21$, the ratio of which radii is, in the limit, $\varphi = (1 + \sqrt{5})/2$. Figure 7 illustrates the locus of all wavevectors with nontrivial amplitudes. The Fibonacci modes, whose amplitudes are indicated by color, are the only modes to approach the preferred wavelength.

These considerations suggest that the quantities we should monitor are the amplitudes and radial wavenumbers of the signal $u(\mathbf{x},t) = \sum_j u_{m_j}(r,t) \exp(-im_j\theta) + (*)$, for a set of integers $\{m_j\}$, which we obtain by writing $u_{m_j}(r,t)$ as $a_{m_j}(r,t) \exp(i\phi_{m_j})$. At any given r and t, the amplitudes are given by the sequence $\{a_{m_j}\}$ and the radial wavenumbers ℓ_{m_j} by $-d\phi_{m_j}/dr$. We also monitor the front speed v, which is not constant but varies in a log periodic fashion over distances separated by φ, the golden number. Because the chosen pattern combines several modes, one has to ask if they can all propagate as a synchronous front. There are two kinds of fronts [14]. The first kind are pulled fronts whose properties are determined by conditions in the unstable state ahead of the front. The second category, to which Fibonacci spirals belong, are pushed fronts whose speeds and steepnesses exceed those of the pulled front and whose characteristics are determined by conditions behind the front. This is essential for Fibonacci patterns because it ensures both that the modes participating in the pattern structure all propagate in synchrony and introduces the
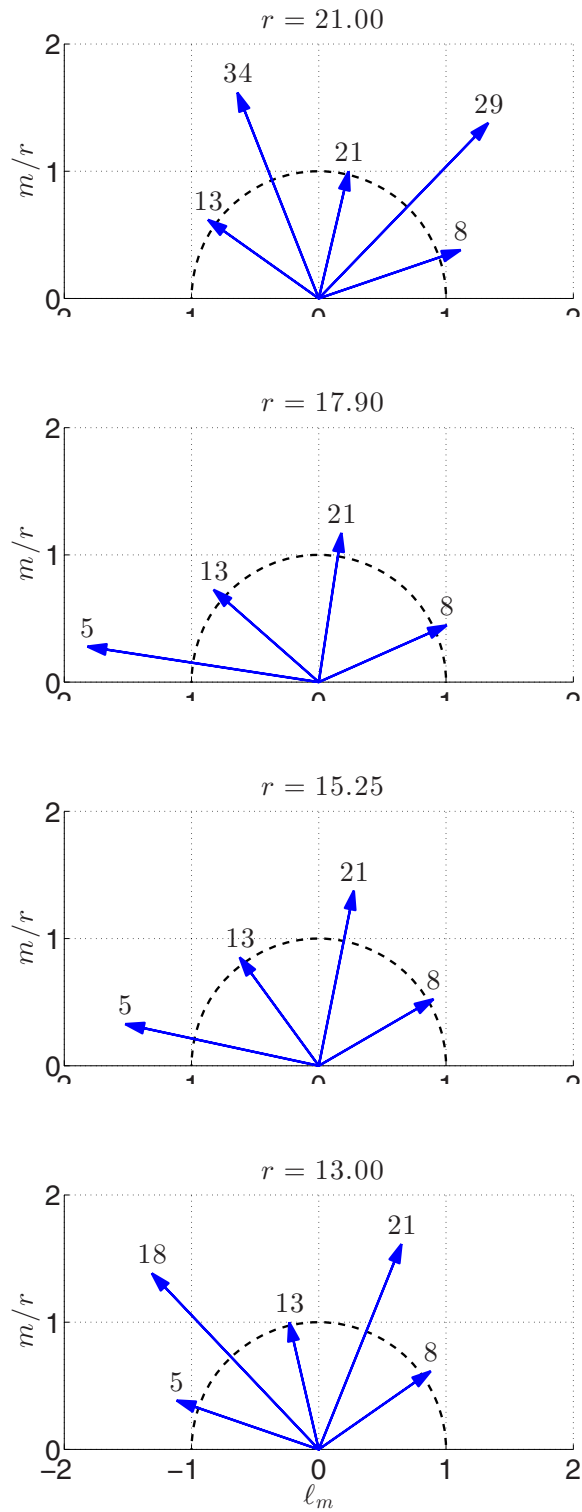
Fig. 6. Wavevectors for modes with amplitude greater than 10% of the maximum value at each the radii listed. The dashed semicircle indicates the most unstable wavelength. A movie may be found at `http://math.arizona.edu/~pennybacker/media/wavevectors/`.
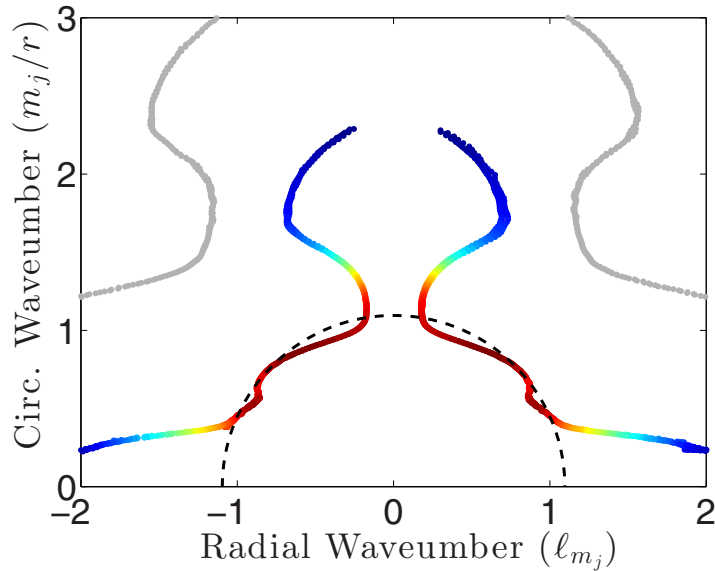
Fig. 7. Inside, the locus of wavevectors for modes with amplitude greater than 10% of the maximum value. The color indicates the amplitude of the mode with that wavevector. Outside, the locus of wavevectors for irregular Fibonacci modes. The dashed semicircle indicates the energetically preferred wavelength.

important ingredient of bias into pattern choice. Namely the choice of pattern emerging in the present generative annulus is influenced by the pattern already laid down in the previous one. This is important because the free energy landscape has many critical points. The 'minimum' which is chosen is the one for which the previous state of the system lies in its basin of attraction. As we have noted, however, the 'minima' corresponding to Fibonacci spirals are weakly unstable states, but their loci on the $(\ell_{m_j}(r), \ell_{m_{j+1}}(r))$ plane are continuous curves so that, as r changes, the pattern changes smoothly. Eventually the Fibonacci pattern generated by (1) will occupy a region large enough so that it will think it is on a plane. Very slowly, it will develop defects which will lead to patches of pure hexagonal planforms mediated by defects. But coarsening takes a long time. Moreover, in plants there may very well be rooting mechanisms which pin the angular positions of primordia once they begin to grow. See further remarks in Section 3.6.

3.2. Why Fibonacci?

We now provide evidence as to how the pushed pattern forming front acts to select Fibonacci sequences.

In Figures 3 and 4, we show the simulations of the patterns generated from (1) starting with parastichy numbers $(89, 144)$ at $r = 233$ and $(76, 123)$ at $r = 199$. We call these $(1, 2)$ and $(1, 3)$ sunflowers respectively, since the starting parastichy numbers are consecutive members of the Fibonacci-like sequence starting with these two values. We use three different sets of starting parastichies to emphasize that it is the Fibonacci addition rule which is important and not any particular sequence. The results we obtain hold for that open set of values in the (μ, β)-plane for which the front is pushed. In the calculations, we use typical values $\mu = 1 \times 10^{-3}$ and $\beta = 3$.

In Figure 5, we show the maximum amplitudes of each circumferential wavenumbers over all radii. One observes that the dominant amplitudes in each case are those members defined by $m_{j+1} = m_{j-1} + m_j$ (or $m_{j-1} = m_{j+1} - m_j$) and starting with the outermost parastichy numbers. That the maxima are of equal value suggests the pattern has self-similar properties. In each case, their second harmonics and those obeying the addition rule $m = m_{j-1} + m_{j+1}$ are also generated by quadratic interactions, but they belong to the passive set $\mathscr{P}(\mathscr{A})$ and their amplitudes are much

smaller than those in the active Fibonacci sequence. All other modes are barely generated at all. Their amplitudes are all less than 2% of the maxima. Figure 6 shows why the selection occurs in that it plots the positions of the wavevectors $\mathbf{k}_j$ as r decreases. We show how the wavevectors in the Fibonacci sequence move towards the critical circle or preferred wavenumber at certain r values whereas those of the passive modes all move away. Because the governing equation is nonlinear in the field gradient, the energetically preferred wavenumber is not the one chosen by linear stability considerations (here $k_0 = 1$) but is instead dependent on the parameter β as

$$k_0 \approx \sqrt{\frac{135 + \beta^2}{135 - 2\beta^2}}.$$

The choice $\beta = 3$ gives $k_0 \approx 1.11$.

In [15], runs are displayed which begin with mixtures of parastichies. In these cases, the different Fibonacci sequences compete for dominance and the pattern will take a long time to settle on one choice. Of course, in sunflowers, the starting configurations are dominated by whichever Fibonacci sequence the flower portion of the plant has chosen. This is usually the regular sequence $2, 3, 5, \ldots$ because, in the flower generation stage, the plant often begins as a decussate $(2, 2, 4)$ and adopts the Fibonacci triad $(2, 3, 5)$ at a generative radius where the decussate solution no longer exists.

3.3. The field amplitudes and self-similarity

In Figure 8, we show, for both sets of starting parastichies, the new amplitude invariant which has no parallel in the discrete algorithms that only generate point configurations. It is a curve drawn as a function of r/φ^j on a logarithmic scale, where j is integer and φ is the golden number $(1 + \sqrt{5})/2$, the limit of the ratio of successive terms of any Fibonacci sequence. Its shape is invariant. The graph for the starting parastichies $(76, 123)$ is phase shifted from that with starting parastichies $(89, 144)$ but is otherwise identical. As r decreases from 233 (199) to 8 (7), the Fibonacci amplitudes $a_{233}, \ldots, a_5, a_3, a_2$ (respectively $a_{199}, \ldots, a_7, a_4, a_3$) move over this curve. In Figure 8, at $r \approx 144$, the configuration is almost hexagonal with a_{144}, a_{89}, a_{55} occupying the positions B, C, D respectively. As r decreases, the amplitude a_{144} will very quickly decrease leaving a_{55} and a_{34} dominant (and almost unchanged) for a short interval until the amplitude a_{21} rises quickly to form the next hexagonal configuration at $r \approx 89$. As r continues to decrease, the pattern repeats with a_{89}, a_{55}, a_{34} and a_{21} replacing a_{144}, a_{89}, a_{55} and a_{34}. The graph of the locus of $\{a_{m_j}\}$ in three dimensions $(a_{m_{j+1}}, a_{m_j}, a_{m_{j-1}})$ is given in Figure 9 and shows a common homoclinic orbit joining the origin to itself with six legs on which there are two-mode dominated transitions from hexagons from circumferential wavenumbers m_{j+1}, m_j, m_{j-1} to m_j, m_{j-1}, m_{j-2}. At every r, we verify that $a_{m_{j+1}}(r\varphi) = a_{m_j}(r)$.

3.4. Lattice configurations

The overall arrangement of phylla on the sunflower head is not a fixed spiral lattice but a slowly varying one. The reason for this is that, at any given radius, the number of preferred wavelengths that fit in the gradually moving annulus decreases. We have seen this already in the case of the amplitudes in Figures 8 and 9. As the radius of the generative annulus (the position of the pushed pattern forming front) decreases, the lower amplitudes in the chosen Fibonacci sequence dominate. So it is with the structure of the lattices on which the field maxima lie. To quantify the changes, we measure at each r the radial wavenumbers $\ell_{m_j}(r) = -\partial \varphi_{m_j}/\partial r$. They vary slowly. Namely they change significantly over distances large compared with the preferred wavelength.

In Figure 13, we show the common locus of the positions of all successive radial wavenumbers $(\ell_{m_j}, \ell_{m_{j+1}})$ as r varies. They all lie on a common curve. The curve undergoes a rapid change in slope at the points marked A, B, C and D. These all correspond to almost hexagonal planforms where three amplitudes of successive Fibonacci modes and their wavenumbers $k_{m_j} = \sqrt{\ell_{m_j}^2 + m_j^2/r^2}$ are approximately equal. They are also the points at which the dominant parastichies change, from (m_{j-1}, m_j) to (m_j, m_{j+1}). If the reader will click on the link in the caption of this figure, he or she can see the points move as r changes. We emphasize that this curve is invariant and is the invariant curve for all Fibonacci sequences no matter what the starting parastichies are. One can also check that, for every j and at every r, $\ell_{m_{j+1}}(r\varphi) = -\ell_{m_j}(r)$.
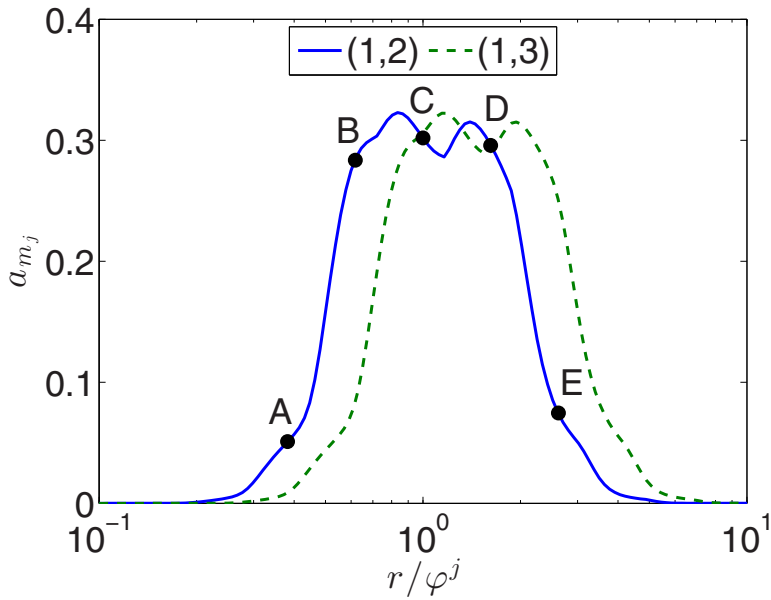
Fig. 8.   The invariant amplitude curve for amplitudes a_{m_j} with m_j from the Fibonacci-like sequences starting with $(1,2)$ and $(1,3)$.   The horizontal scaling emphasizes the self-similar property $a_{m_j}(r) = a_{m_{j+1}}(\varphi r)$.   A movie may be found at http://math.arizona.edu/~pennybacker/media/amplitude/.
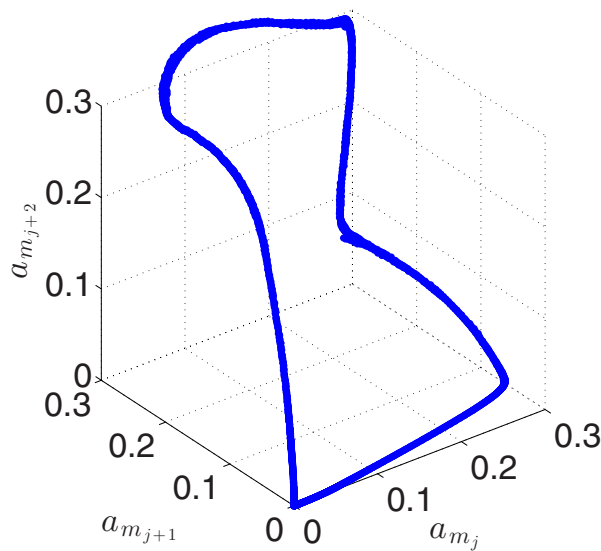

Fig. 9.   The phase space of amplitude triads $(a_{m_j}, a_{m_{j+1}}, a_{m_{j+2}})$ with m_j from the Fibonacci-like sequences starting with $(1,2)$ and $(1,3)$.   Each triple evolves along a homoclinic orbit starting and ending at $(0,0,0)$.   A movie may be found at http://math.arizona.edu/~pennybacker/media/amplitudetriads/
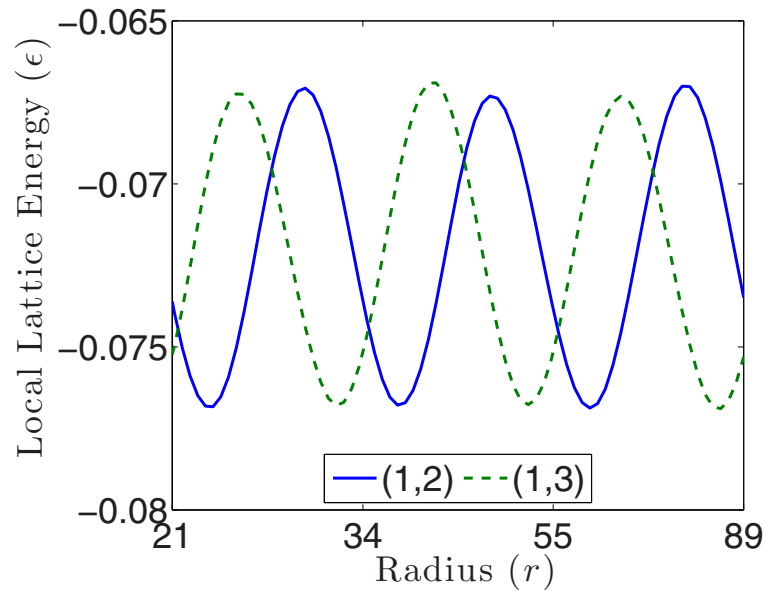
Fig. 10. The local energy ε for the $(1,2)$ and $(1,3)$ sunflowers.
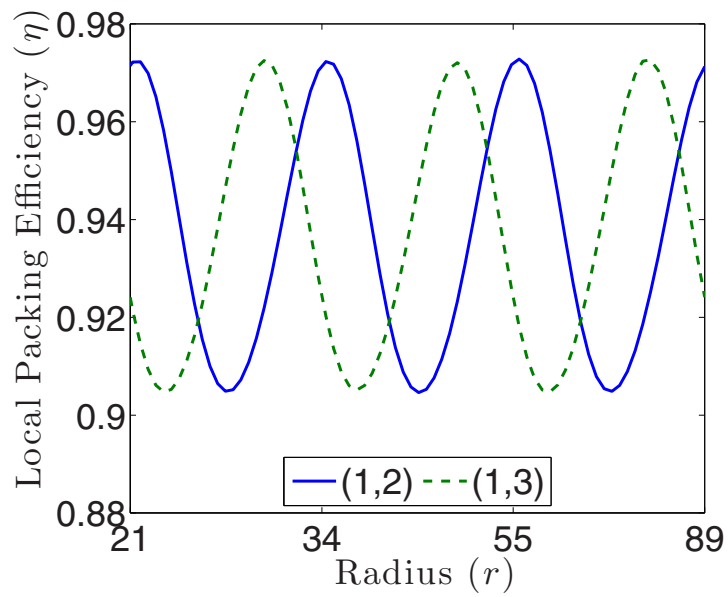

Fig. 11. The local packing efficiency η for the $(1,2)$ and $(1,3)$ sunflowers.
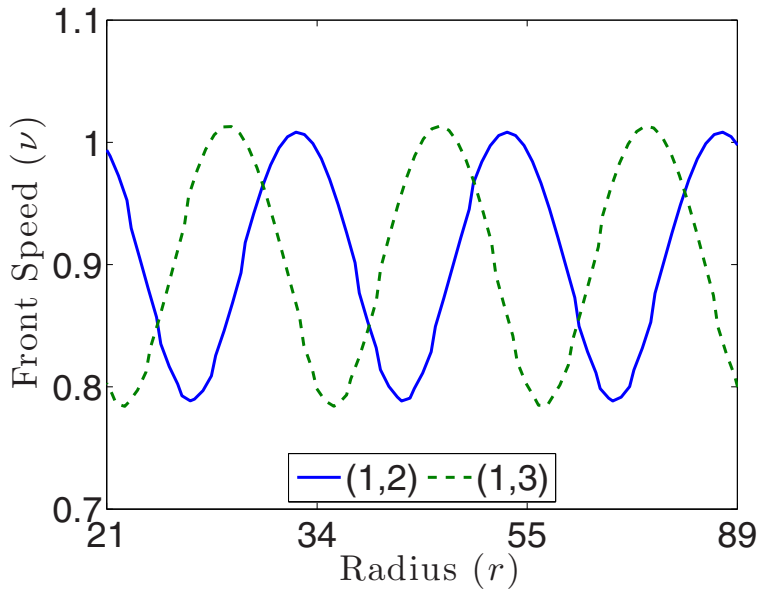
Fig. 12. The front speed ν for the $(1,2)$ and $(1,3)$ sunflowers.

In Figures 14 and 15, we make contact with the divergence angle versus rise graphs familiar from the analysis of discrete models of phyllotaxis. To do this, we calculate from the radial wavenumbers $(\ell_{m_j}, \ell_{m_{j+1}})$ of the two dominant modes the values of the corresponding divergence angle $\delta(r)$ and rise $\rho(r)$ (the distance between two successive levels of configuration points). To achieve this map, we take advantage of the fact that all of the quantities are slowly varying and assign, at a given radius r, the lattice (defined by $\delta(r)$ and $\rho(r)$) corresponding to that drawn on a cylinder of constant radius r. The maxima of our field lie on two lines given by the local equations $\ell_m z + m\theta = 2\pi p$ and $\ell_n z + n\theta = 2\pi q$ where p and q are integers. We solve these two equations for

$$z = 2\pi \frac{pn - qm}{\ell_m n - \ell_n m},$$
$$\theta = 2\pi \frac{\ell_n q - \ell_m p}{\ell_m n - \ell_n m}.$$

Since m and n are coprime, we can always find p and q such that $pn - qm = \pm 1$. There are infinitely many possible choices, but we choose the ones which make $0 \le \theta < 2\pi$. This choice of minimal θ is the divergence angle δ. We normalize the radial distance between successive primordia by taking the base of our local cylinder at radius r to have unit circumference. Thus

$$\rho = \frac{1}{r} \frac{pn - qm}{\ell_m n - \ell_n m}.$$

We now plot the pair (ρ, δ) for each r using the data drawn from the field $u(\mathbf{x}, t)$ corresponding to the two sets of starting parastichies. On the background of this graph, we draw the usual Van Iterson diagram whose origin, and whose relation to the discrete dynamical system studied in [12], was discussed in Section 2.

The reader can see that the overlap between the two sets of curves is stunning. The fact that the curves derived from the field maxima laid down by the pushed pattern forming front are slightly different is due to the fact that the field $u(\mathbf{x}, t)$ is not exactly supported on only the Fibonacci modes but has very small remnants of the other dynamically generated modes present in its function space. This is consistent with the numerical experiments of Douady and Couder [9, 10, 11] and Levitov [6].
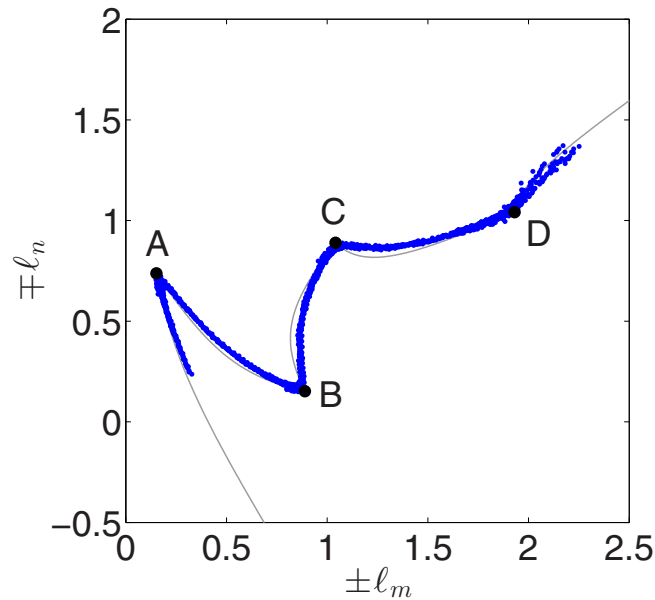
Fig. 13.   The invariant curve in the (ℓ_m, ℓ_n) wavevector space with m and n consecutive members of the appropriate Fibonacci-like sequence.   The data have been reflected so that they all lie in the same quadrant.   The shaded lines are the locus of rhombic lattices with the preferred wavelength along any single branch of the Van Iterson diagram.   A movie may be found at http://math.arizona.edu/~pennybacker/media/wavevectorpairs/.

These results vividly demonstrate that point configurations generated by algorithms based on "least crowded space" optimal packing criteria can be equally well generated by pushed pattern forming fronts which emerge from a mechanistic description of the physics and biochemistry at work in the formation of a plant's phylla. To again quote D'Arcy Thompson, "Like warp and woof, mechanism and teleology are interwoven together, and we must not cleave to the one and despise the other."

The exciting possibility emerging from this realization is that organisms may follow optimal strategies as a result of pattern forming and self-organizing behaviors in many natural contexts.

3.5. Energy and packing densities, front speeds, and the connections between variables associated with two different Fibonacci sequences

In Figures 10, 11 and 12, we show how $\varepsilon(r)$, $\eta(r)$ and $\nu(r)$, the local energy, local packing density and front speed respectively, change with r. The local energy ε is the energy density of the local lattice, computed with the amplitudes and wavevectors measured at each radius. The local packing efficiency η is the largest fraction of the local cylinder, representing the pattern in a narrow annulus at radius r, that can be covered by identical circles centered at maxima of the local lattice. When the pattern is nearly hexagonal, the local energy is low and both the front velocity and local packing efficiency are high. When the pattern is two-mode dominated, but less hexagonal, the opposite is true. Recent experimental work [16] on masking developing seed patterns in sunflowers suggests that it may be possible to measure ν and check that it varies as predicted.

We observe that the graphs for the two cases with parastichies $2, 3, 5, \ldots$ and $1, 3, 4, \ldots$ are identical except for a phase shift. There is a map between the amplitudes, radial wavenumbers and energy densities of any two different Fibonacci sequences. Denoting the standard Fibonacci sequence by $\{f_j\}_{j=1}^{\infty}$ where $f_1 = f_2 = 1$, any Fibonacci-like sequence $\{m_j\}_{j=1}^{\infty}$ generated by integers m_1, m_2 may be written as $m_{j+2} = f_j m_1 + f_{j+1} m_2$. For any two Fibonacci-like
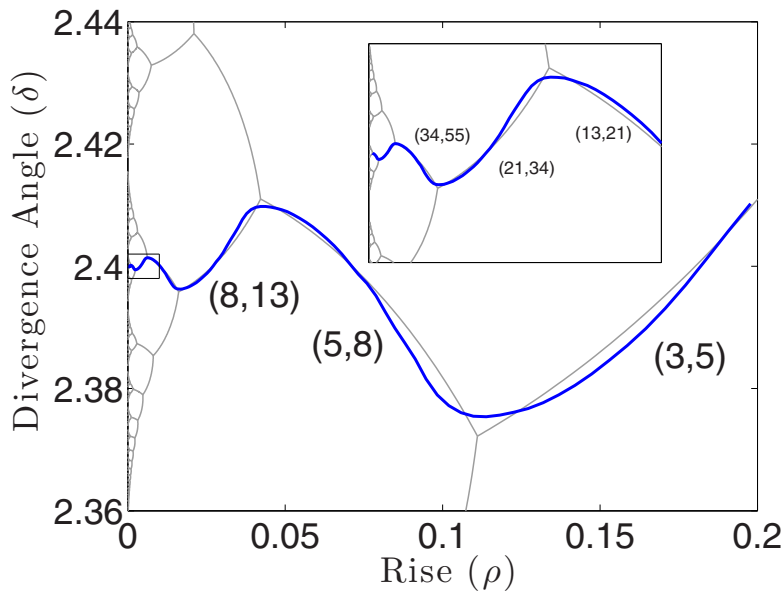
Fig. 14. The rise ρ and divergence angle δ given by the local lattice structure at each radius on the $(1,2)$ sunflower. The shaded lines are the van Iterson tree, with selected parastichy pairs indicated. Inset is detail of the data for small ρ. A movie may be found at `http://math.arizona.edu/˜pennybacker/media/divergence/`.
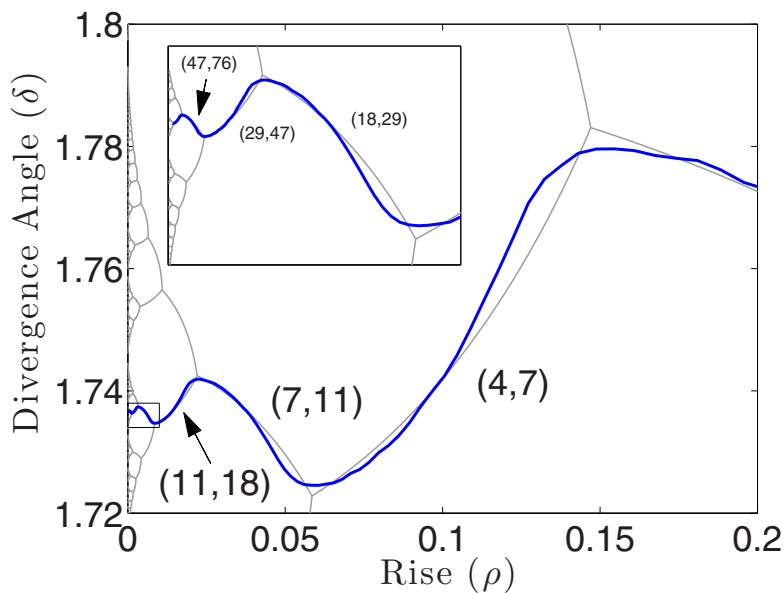

Fig. 15. The rise ρ and divergence angle δ given by the local lattice structure at each radius on the $(1,3)$ sunflower. The shaded lines are the van Iterson tree, with selected parastichy pairs indicated. Inset is detail of the data for small ρ.
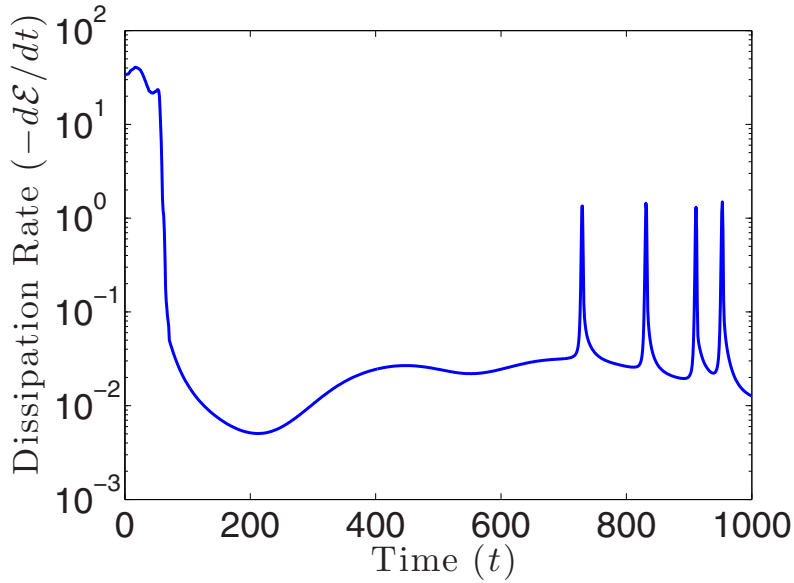
Fig. 16. The long-time dissipation rate on the annulus $34 < r < 55$. The initially large value is due to the formation of the Fibonacci pattern. It is followed by a rapid decrease in energy dissipation and for a long period the energy remains approximately constant. Then, as defects form, there are sharp peaks, eack peak corresponding to the formation of a defect.

sequences $\{m_j\}$ and $\{n_j\}$, therefore

$$\frac{n_{j+2}}{m_{j+2}} = \frac{f_j n_1 + f_{j+1} n_2}{f_j m_1 + f_{j+1} m_2}$$

$$= \frac{n_1 + \frac{f_{j+1}}{f_j} n_2}{m_1 + \frac{f_{j+1}}{f_j} m_2} \rightarrow \frac{n_1 + \varphi n_2}{m_1 + \varphi m_2} = \varphi_{mn}.$$

Hence,

$$\frac{m_j}{r} \simeq \frac{n_j}{r \varphi_{mn}}$$

Now consider two Fibonacci-like sequences $\{m_j\}$ and $\{n_j\}$ and corresponding energies $\varepsilon_m = \varepsilon(\{a_j\}, \ell_1, \ell_2; \{m_j/r\})$ and $\varepsilon_n = \varepsilon(\{b_j\}, \ell_1', \ell_2'; \{n_j/r\})$ given by projecting the energy function (2) onto the respective Fibonacci basis modes and averaging. We will take the generators of all radial wavenumbers to be ℓ_1, ℓ_2 and ℓ_1', ℓ_2' respectively with $\ell_{j+2} = f_j \ell_1 + f_{j+1} \ell_2$. For a given value of r, suppose that $\{a_j(r)\}, \ell_1(r), \ell_2(r)$ give a local minimum of ε_m. Then, ε_n is minimized by variables $b_j(r\varphi_{mn}) \simeq a_j(r), |\ell_1'(r\varphi_{mn})| \simeq |\ell_1(r)|, |\ell_2'(r\varphi_{mn})| \simeq |\ell_2(r)|$.

3.6. Long-time dynamics

As mentioned previously, the Fibonacci pattern is not globally stable on the disc, but instead relaxes slowly to a planar hexagonal pattern. To investigate the time scales involved in this phenomenon, we excise the annulus $34 < r < 55$ from the simulation of the full sunflower head and allow it to evolve under (1) for 1000 time units. A key quantity that we use to study how quickly the pattern evolves is the dissipation rate

$$-\frac{d\mathcal{E}}{dt} = -\int \frac{\delta \mathcal{E}}{\delta u} \frac{\partial u}{\partial t} = \int \left(\frac{\delta \mathcal{E}}{\delta u}\right)^2,$$

a measure of the energy gradient about the solution. Computed values of the dissipation rate are shown in Figure 16.

For $t < 50$, the pushed front is propagating through the annular domain, so the energy gradient is large and is concentrated about the transition region. Note that the dissipation rate fluctuates due to the difference in energy between hexagonal and rhombic regions; the maximum occurs when the front is propagating through the most hexagonal region. Once the front has left the domain, the dissipation rate falls by more than three orders of magnitude. For $50 < t < 300$, the dynamics are dominated by a very weakly unstable trajectory that does not change the overall planform. For $t > 300$, global reorganization of the planform begins to occur. Rhombic regions develop into hexagonal patches separated by phase grain boundaries. The reorganization also opens up gaps in the planform which eventually become defects after the formation of a new maximum. These events appear as sharp peaks in the dissipation rate starting at $t \approx 700$.

We make two observations regarding these results. First, the time scale of global reorganization is much longer than the time that it takes for the pattern to be fully laid down by the front. The Fibonacci pattern is therefore a saddle point in the energy landscape more closely resembling a canyon. The front provides a mechanism for the system to rapidly reduce its energy, with the price being a bias imposed by the pattern already laid down in the vicinity of the transition region. Second, it is not unreasonable to expect that there is a change in the mechanism of morphogenesis once a primordium has been initiated. In particular, there may be a way for young primordia to fix their position on the plant. Our results indicate that this process would not need to occur immediately after formation. It would only need to be faster than the global reorganization time scale in order to preserve the planform.

At this stage we can be a bit more precise about what we meant by critical points and minima in inverted commas. If we fix the variable radius in (1) and look at the evolution of a pattern on a cylinder, we find the following. For a countable set of r values, each corresponding to a parastichy pair, the hexagon state fits on the cylinder just as it does in the leftmost frames in Figure 1. Its evolution remains a hexagon for all time. Moreover, if we start with a perturbation of the hexagon state at these r values, the pattern relaxes strongly to the hexagon state. It is indeed stable. If we do the same experiment at a slightly larger radius than one of those special few r values, biasing the outcome by choosing a previous hexagon state as an initial condition, we find that the pattern relaxes to the rhombic state evident throughout the transition regions in Figures 3 and 4. But it does not remain there for long times. It is weakly unstable. It is in fact a saddle with a strongly attracting stable manifold and a weakly repelling unstable one. Of course, on the disc, the r value is continuously changing and so the Fibonacci pattern from $r = 203$ down to $r = 8$ is formed and is seemingly stable before the weak instabilities associated with the rhombic states make their appearance. Thus the whole Fibonacci pattern is weakly unstable because its weakest links, its rhombic forms, are weakly unstable. But as we have speculated, in situations where such weakly unstable patterns might appear in nature, in plants or as seashells, the Fibonacci pattern becomes rooted or pinned or the seashell hardens before the potential instability is able to express itself.

3.7. Whorls

Whorl structures are solutions supported on modes with wavenumbers $(\pm \ell, m)$ and $(0, 2m)$. These would correspond to non-simple lattices for which one of the principal hexagonal axes is parallel to the axis of the cylinder and more than one lattice point lies at each level. They exist only for finite ranges of radii. Many plants begin their phyllotactic configurations as decussates for which $m = 2$ and ℓ is chosen to minimize the energy. For the most part, this means that the three wavenumbers $\sqrt{\ell^2 + m^2/r^2}$ and $2m/r$ have the preferred value and that their amplitudes are nearly equal, an almost hexagonal configuration. In the left of Figure 17, we show the lattice structure for a whorl on a cylinder of radius r. Then we slowly increase r. At a certain radius, the whorl solution ceases to exist. What happens is that the chiral symmetry is broken and the whorl structure is replaced by a $(2, 3, 5)$ spiral as shown in the right of Figure 17. The transition is achieved by means of an Eckhaus-like instability in which two of the four maxima associated with the $m = 4$ mode separate more than the others and a new maximum is inserted.

For the most part, as the radius is further increased, the $(2, 3, 5)$ spiral structure evolves up the regular Fibonacci sequence. But there are examples of plants which appear to alternate and adopt the transition sequence $(2, 2, 4) \rightarrow (2, 3, 5) \rightarrow (3, 3, 6) \rightarrow (3, 4, 7) \rightarrow (4, 4, 8)$ as the radius continues to increase. As of this time, we do not know the reason that a plant would choose to evolve in this fashion over evolving along a regular Fibonacci sequence. Indeed, the details of transitions between whorls and Fibonacci spirals or between different families of Fibonacci spirals (all
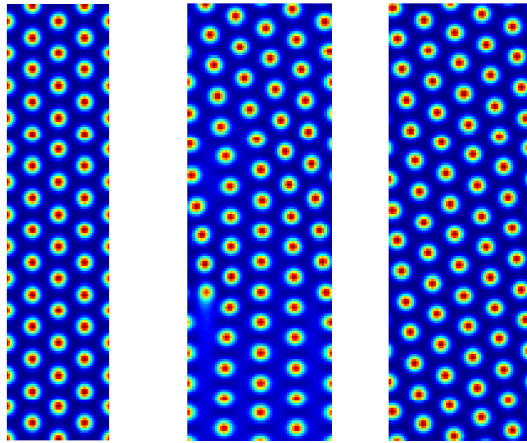
Fig. 17. A pseudocolor plot of $u(\mathbf{x},t)$ on a cylinder illustrating a whorl-to-spiral transition. Left to right: A stable 2-whorl pattern, the instability of the 2-whorl to a $(2,3)$ spiral after a change in radius and the stable $(2,3)$ spiral pattern at the larger radius.

order-one phase transitions) is still an open challenge.

4. Conclusions

What this paper has demonstrated is very exciting because it suggests how nature can follow optimal strategies by using self organized patterns which arise by stressing systems far from equilibrium. The self organized patterns involve length scales which are of the same order as those observed so that no staircase of actions initiated by DNA sized scales nor explanations based on teleology are required to gain understanding. The credibility and robustness of the results, which follow spiral patterns making smooth transitions through many parastichy pairs, from $(89, 144)$ down to $(3,5)$, are due in no small measure to the numerical algorithm which was the brainchild of the second author and which is spelled out in detail in his thesis.

Besides the question raised in Section 3.7, there are many exciting open challenges which remain. We will briefly discuss three. First, it is intriguing to ask why an equation such as (1) has solutions which exhibit so many symmetries and invariants. These are probably not properties which can be derived from the equation itself but are properties rather of the projection of the solution into the subset of active modes, here Fibonacci, which dominate the dynamics because of reasons we have discussed. This introduces a novel question in the analysis of PDE's. It is known, for example, that many special solutions of PDE's, the ODE's that describes its traveling wave solutions, can be integrable whereas the original PDE is not. How might one go about teasing out the fact that certain dominant special solutions of a given PDE has all these hidden symmetries?

Second, it is natural to ask about the universality of Fibonacci patterns. The two crucial ingredients in their ubiquity in plants are that the system has a broken sign reversal symmetry and that the pattern is laid down annulus by annulus. The first ingredient ensures that quadratic interactions which add the phases of periodic active modes are important. This is a necessary requirement for the Fibonacci rule. The second ingredient, the fact that the pattern is laid down annulus by annulus and not all at once over the plane means that the energy landscape minimum chosen will be heavily influenced by the nature of the pattern in the previously laid down annulus. This helps the spiral phyllotaxis minimum win over a minimum in which the plane is uniformly tiled with hexagons.

Because neither of these ingredients are necessarily exclusive to plants, there should be many other physical contexts in which spiral phyllotaxis patterns are seen. Indeed, Levitov [6] demonstrated that in certain circumstances they could be observed in superconductors. One of the authors of this paper is working with a group in Göttingen to see if a convection experiment could be induced to display such patterns. Eventually of course, as we have already said, they

will succumb to noise and tunnel their way back to a pattern consisting of patches of hexagons mediated by defect points and lines. But that can take a long time so that it is not unreasonable to expect them to be seen as metastable states in many places.

Third, it is also natural to ask what might be the dominant rule if a three dimensional pattern were to be laid down annulus by annulus in a spherical geometry. In this case, the phases of the active modes would contain two integer wavenumbers corresponding to the longitude and latitude directions. If we were to use the same governing equation, what might be the addition rule which leads to the dominant pattern seen in such a situation?

References

[1] Newell AC, Shipman PD, Sun Z. Phyllotaxis: cooperation and competition between mechanical and biochemical processes. J Theor Biol. 2008 Apr;251(3):421–39.

[2] Jönsson H, et al. An auxin-driven polarized transport model for phyllotaxis. Proc Natl Acad Sci USA. 2006 Jan;103(5):1633–8.

[3] Reinhardt D, et al. Regulation of phyllotaxis by polar auxin transport. Nature. 2003 Nov;426(6964):255–60.

[4] Green PB, Steele CS, Rennich SC. How plants produce patterns. A review and a proposal that undulating field behavior is the mechanism. In: Jean RV, Barabé D, editors. Symmetry in Plants. Singapore: World Scientific; 1998. p. 359 – 392.

[5] van Iterson I. Mathematische und Mikroskopisch-Anatomische Studien über Blattstellungen nebst Betrachtungen über den Schalenbau der Miliolinen. Jena: Gustav Fischer; 1907.

[6] Levitov L. Phyllotaxis of Flux Lattices in Layered Superconductors. Phys Rev Lett. 1991;66(2):224–227.

[7] Hofmeister W. Allegmeine Morphologie der Gewachse. Handbuch der Physiologischen Botanik. Leipzig: Engelmann; 1868.

[8] Snow M, Snow R. Minimum areas and leaf determination. Proc R Soc B. 1952;139:545–566.

[9] Douady S, Couder Y. Phyllotaxis as a dynamical self organizing process part I: the spiral modes resulting from time-periodic iterations. Journal of theoretical biology. 1996;p. 255–274.

[10] Douady S, Couder Y. Phyllotaxis as a dynamical self organizing process Part II: the spontaneous formation of a periodicity and the coexistence of spiral and whorled patterns. Journal of theoretical Biology. 1996;p. 275–294.

[11] Douady S, Couder Y. Phyllotaxis as a dynamical self organizing process Part III: The simulation of the transient regimes of ontogeny. Journal of theoretical Biology. 1996;p. 295–312.

[12] Atela P, Golé C, Hotton S. A Dynamical System for Plant Pattern Formation: A Rigorous Analysis. J Nonlinear Sci. 2003 Jan;12(6):641–676.

[13] Shipman PD, Sun Z, Pennybacker M, Newell AC. How Universal Are Fibonacci Patterns? EPJ D. 2010;62:5–17.

[14] Van Saarloos W. Front propagation into unstable states. Physics Reports. 2003 Nov;386(2-6):29–222.

[15] Pennybacker M. A Numerical Study of Pattern Forming Fronts in Phyllotaxis. University of Arizona. Tucson; 2013.

[16] Hotton S, et al. The Possible and the Actual in Phyllotaxis: Bridging the Gap between Empirical Observations and Iterative Models. J Plant Growth Regul. 2006 Nov;25(4):313–323.

[17] Furihata D, Matsuo T. Discrete Variational Derivative Method. Chapman and Hall/CRC; 2010.

Appendix A. Numerical methods

An important tool for our exploration of (1) is an efficient, accurate and stable numerical method. The most commonly used methods for this class of problem exploit a spectral decomposition of one form or another. Unfortunately, the geometry and inhomogeneity of the pattern-forming front conspire to make such methods impractical. We have instead chosen a finite difference scheme based on the Discrete Variational Derivative Method of Furihata and Matsuo [17].

A.1. Preliminaries

We present our method in one spatial dimension so as to simplify the following discussion; its extension to two spatial dimensions is straightforward.

Let $\mathbf{u}_k^m \approx u(k\Delta x, m\Delta t)$ be an approximate solution of (1) on a regular grid with spacings Δx and Δt. We adopt somewhat standard notation for the forward and backward first difference operators

$$\delta^+ \mathbf{f}_k = \frac{\mathbf{f}_{k+1} - \mathbf{f}_k}{\Delta x}, \qquad \delta^- \mathbf{f}_k = \frac{\mathbf{f}_k - \mathbf{f}_{k-1}}{\Delta x},$$

and the centered first and second difference operators

$$\delta^{\langle 1 \rangle} \mathbf{f}_k = \frac{\mathbf{f}_{k+1} - \mathbf{f}_{k-1}}{2\Delta x}, \qquad \delta^{\langle 2 \rangle} \mathbf{f}_k = \frac{\mathbf{f}_{k+1} - 2\mathbf{f}_k + \mathbf{f}_{k-1}}{(\Delta x)^2}.$$

We also use the notation

$$\overline{\sum_k} \mathbf{f}_k = \frac{\Delta x}{2} \left(\mathbf{f}_0 + \mathbf{f}_N + 2 \sum_{k=1}^{N-1} \mathbf{f}_k \right)$$

to represent the trapezoidal sum of $\mathbf{f}$. Finally, we will exploit the summation by parts formula

$$\overline{\sum_k} \mathbf{f}_k (\delta^+ \mathbf{g}_k) + \overline{\sum_k} (\delta^- \mathbf{f}_k) \mathbf{g}_k = h(\mathbf{f}, \mathbf{g})$$

where the right-hand-side depends only on boundary terms of $\mathbf{f}$ and $\mathbf{g}$, and whose explicit formula is given in [17]. This is exactly the discrete analogue of integration by parts.

A.2. The basics

From the variational formulation of (1) we immediately obtain the dissipation property

$$\frac{d}{dt} \mathscr{E}[u] \leq 0.$$

Our goal is to enforce this property up to truncation error, but to do so requires the introduction of some new machinery. In particular, we need a discrete formulation of the variational derivative.

Let us begin by constructing a (useless) semi-discrete numerical method. Lacking an infinitesimal span of time, we must be able to approximate the variational derivative using values of the solution at two different times. Recall that the variational derivative of a functional $\mathscr{E} : M \to \mathbb{R}$ defined by a definite integral is the function $\delta\mathscr{E}/\delta u$ such that

$$\int \frac{\delta\mathscr{E}}{\delta u} v \, dx = \lim_{\varepsilon \to 0} \frac{\mathscr{E}[u + \varepsilon v] - \mathscr{E}[u]}{\varepsilon}$$

for all $v \in M$. Unable to take the limit, we settle for a fixed but small value of ε, and so an approximation to $\delta\mathscr{E}/\delta u$ given a 'nearby' function v is the function $\delta\mathscr{E}/\delta(v, u)$ such that

$$\int \frac{\delta\mathscr{E}}{\delta(v, u)} (v - u) \, dx = \mathscr{E}[v] - \mathscr{E}[u].$$

In some sense, this approximation is the result of 'dividing' the difference in function values $v - u$ out of the difference in functional values $\mathscr{E}[v] - \mathscr{E}[u]$. For example, consider the free energy for classical solutions to the diffusion equation given by

$$\mathscr{E}[u] = -\frac{1}{2} \int u_x^2 \, dx.$$

We may compute

$$
\begin{aligned}
\mathscr{E}[v] - \mathscr{E}[u] &= -\frac{1}{2} \int \left(v_x^2 - u_x^2 \right) dx \\
&= -\frac{1}{2} \int (v_x + u_x)(v_x - u_x) \, dx \\
&= \frac{1}{2} \int (v_{xx} + u_{xx})(v - u) \, dx
\end{aligned}
$$

using integration by parts, ensuring that the boundary terms disappear. Consequently,

$$\frac{\delta \mathscr{E}}{\delta(v,u)} = \frac{1}{2}(v_{xx} + u_{xx})$$

which reduces to $\delta \mathscr{E}/\delta u$ when $v = u$. Now we are ready to construct the semi-discrete method. Let $u^m(x) \approx u(x, m\Delta t)$ be an approximate solution of the (very general) partial differential equation

$$\frac{\partial u}{\partial t} = -\frac{\delta \mathscr{E}}{\delta u}$$

at values of time separated by Δt. It follows naturally that we take

$$\frac{u^{m+1} - u^m}{\Delta t} = -\frac{\delta \mathscr{E}}{\delta(u^{m+1}, u^m)}$$

as our method. This yields an ordinary differential equation to be solved implicitly for $u^m(x)$ at each time step. Notice that we are guaranteed

$$\mathscr{E}[u^{m+1}] - \mathscr{E}[u^m] \leq 0$$

given appropriate boundary conditions and so our goal is achieved.

In order to construct a fully-discrete numerical method, we must trade a functional acting on a function space for a function acting on a vector space. Let $E : V \to \mathbb{R}$ be an approximation to the functional $\mathscr{E}$. That is, replace the integral with a sum and the continuous derivatives with finite differences. The particular discretization is not important, so long as it satisfies certain criteria which are necessary to maintain the order of the method. See [17] for details.

We define the discrete variational derivative to be the vector $\delta E/\delta(\mathbf{v}, \mathbf{u})$ such that

$$\overline{\sum_k} \frac{\delta E}{\delta(\mathbf{v}, \mathbf{u})_k} (\mathbf{v}_k - \mathbf{u}_k) = E(\mathbf{v}) - E(\mathbf{u}).$$

Returning to the diffusion equation, suppose we take

$$E(\mathbf{u}) = -\frac{1}{4} \overline{\sum_k} \left((\delta^- \mathbf{u}_k)^2 + (\delta^+ \mathbf{u}_k)^2 \right).$$

A straightforward computation yields

$$
\begin{aligned}
E(\mathbf{v}) - E(\mathbf{u}) &= -\frac{1}{4} \overline{\sum_k} \left[\left((\delta^- \mathbf{v}_k)^2 + (\delta^+ \mathbf{v}_k)^2 \right) - \left((\delta^- \mathbf{u}_k)^2 + (\delta^+ \mathbf{u}_k)^2 \right) \right] \\
&= \frac{1}{2} \overline{\sum_k} \left(\delta^{\langle 2 \rangle} \mathbf{v}_k + \delta^{\langle 2 \rangle} \mathbf{u}_k \right) (\mathbf{v}_k - \mathbf{u}_k)
\end{aligned}
$$

using summation by parts, ensuring that the boundary terms disappear. So

$$\frac{\delta E}{\delta(\mathbf{v}, \mathbf{u})_k} = \frac{1}{2}\left(\delta^{\langle 2 \rangle}\mathbf{v}_k + \delta^{\langle 2 \rangle}\mathbf{u}_k\right).$$

Finally, let us construct the fully-discrete method by taking

$$\frac{\mathbf{u}_k^{m+1} - \mathbf{u}_k^m}{\Delta t} = -\frac{\delta E}{\delta(\mathbf{u}^{m+1}, \mathbf{u}^m)_k}.$$

This yields an implicit method that is second-order in both time and space. For the diffusion equation, it is exactly the Crank-Nicholson scheme. Notice that we are guaranteed

$$E(\mathbf{u}^{m+1}) - E(\mathbf{u}^m) \leq 0$$

given appropriate boundary conditions. Now, we have the tools to construct a numerical method that automatically satisfies this discrete analog of the dissipation property.

A.3. The method

For (1), we take

$$E(\mathbf{u}) = \sum_k \left[\frac{1}{2}A(\mathbf{u})_k - \frac{\beta}{6}B(\mathbf{u})_k + \frac{1}{4}C(\mathbf{u})_k\right]$$

where

$$A(\mathbf{u})_k = (\delta^{\langle 2 \rangle}\mathbf{u}_k)^2 - (\delta^+\mathbf{u}_k)^2 - (\delta^-\mathbf{u}_k)^2 + (1-\mu)(\mathbf{u}_k)^2$$
$$B(\mathbf{u})_k = \mathbf{u}_k\left((\delta^-\mathbf{u}_k)^2 + (\delta^+\mathbf{u}_k)^2\right)$$
$$C(\mathbf{u})_k = (\mathbf{u}_k)^4$$

The resulting discrete variational derivative is given by

$$\frac{\delta E}{\delta(\mathbf{v}, \mathbf{u})_k} = \frac{1}{2}\mathscr{A}(\mathbf{v}, \mathbf{u})_k - \frac{\beta}{6}\mathscr{B}(\mathbf{v}, \mathbf{u})_k - \frac{1}{4}\mathscr{C}(\mathbf{v}, \mathbf{u})_k$$

where

$$\mathscr{A}(\mathbf{v}, \mathbf{u})_k = \left[\mu - (1 + \delta^{\langle 2 \rangle})^2\right](\mathbf{v}_k + \mathbf{u}_k)$$
$$\mathscr{B}(\mathbf{v}, \mathbf{u})_k = \mathbf{u}_k(\delta^{\langle 2 \rangle}\mathbf{u}_k) + \mathbf{v}_k(\delta^{\langle 2 \rangle}\mathbf{v}_k) + \delta^{\langle 2 \rangle}(\mathbf{u}_k\mathbf{v}_k)$$
$$\mathscr{C}(\mathbf{v}, \mathbf{u})_k = (\mathbf{v}_k)^3 + (\mathbf{v}_k)^2\mathbf{u}_k + \mathbf{v}_k(\mathbf{u}_k)^2 + (\mathbf{u}_k)^3.$$

We then construct the fully-discrete method as before, taking

$$\frac{\mathbf{u}_k^{m+1} - \mathbf{u}_k^m}{\Delta t} = -\frac{\delta E}{\delta(\mathbf{u}^{m+1}, \mathbf{u}^m)_k}.$$

All of the aforementioned simulations have been performed using this method on an annular region centered on the front, tracking its motion and adjusting the domain accordingly. The width of the annulus was chosen large enough that there is no influence on the front from the boundary. See [15] for details.